Article

Landau quantization and highly mobile fermions in an insulator

https://doi.org/10.1038/s41586-020-03084-9

Received: 24 November 2019

Accepted: 21 October 2020

Published online: 4 January 2021

Check for updates

Pengjie Wang[1,6], Guo Yu[1,2,6], Yanyu Jia[1,6], Michael Onyszczak[1], F. Alexandre Cevallos[3], Shiming Lei[3], Sebastian Klemenz[3], Kenji Watanabe[4], Takashi Taniguchi[5], Robert J. Cava[3], Leslie M. Schoop[3] & Sanfeng Wu[1]✉

In strongly correlated materials, quasiparticle excitations can carry fractional quantum numbers. An intriguing possibility is the formation of fractionalized, charge-neutral fermions—for example, spinons[1] and fermionic excitons[2,3]—that result in neutral Fermi surfaces and Landau quantization[4,5] in an insulator. Although previous experiments in quantum spin liquids[1], topological Kondo insulators[6–8] and quantum Hall systems[3,9] have hinted at charge-neutral Fermi surfaces, evidence for their existence remains inconclusive. Here we report experimental observation of Landau quantization in a two-dimensional insulator, monolayer tungsten ditelluride (WTe_2), a large-gap topological insulator[10–13]. Using a detection scheme that avoids edge contributions, we find large quantum oscillations in the material's magnetoresistance, with an onset field as small as about 0.5 tesla. Despite the huge resistance, the oscillation profile, which exhibits many periods, mimics the Shubnikov–de Haas oscillations in metals. At ultralow temperatures, the observed oscillations evolve into discrete peaks near 1.6 tesla, above which the Landau quantized regime is fully developed. Such a low onset field of quantization is comparable to the behaviour of high-mobility conventional two-dimensional electron gases. Our experiments call for further investigation of the unusual ground state of the WTe_2 monolayer, including the influence of device components and the possible existence of mobile fermions and charge-neutral Fermi surfaces inside its insulating gap.

Bulk WTe_2 is a compensated semimetal in which an equal number of electrons and holes coexist[14]. The semimetallic behaviour remains when the material is thinned down to a trilayer[11,15]. In bilayers and monolayers, nevertheless, an insulating gap is observed[11], giving rise to the high-temperature quantum spin Hall effect in monolayers[10–13]. However, the mechanism of the gap opening remains mysterious[10,11,16,17]. The observation of superconductivity when the monolayer is doped with a low electron density[18,19] highlights the unusual nature of the insulating state.

Device design and the insulator state

The design of our devices for investigating the insulating state of monolayer WTe_2 is illustrated in Fig. 1a. A key aim is to detect only the bulk conductance of the monolayer, which we achieve by avoiding contributions from edge states. This is done by inserting a thin insulating layer of hexagonal boron nitride (hBN) between the palladium electrodes and the monolayer; selected small areas of the thin hBN are then etched away so that the tips of the electrodes are in contact with bulk monolayer alone, without touching its edges. We employ a bottom contact geometry, which allows for the preparation of pre-patterned electrodes before the monolayer exfoliation, minimizing the monolayer's degradation. In a completed device, monolayer WTe_2 is encapsulated by top and bottom hBN layers, which also serve as gate dielectrics. An optical image of a typical device is shown in Fig. 1a inset. Detailed fabrication procedures are described in Methods, Extended Data Fig. 1 and Supplementary Information sections S1 and S2.

Figure 1b plots the two-probe resistance R of device 1 as a function of the top-gate voltage V_{tg} while the bottom gate is grounded ($V_{bg} = 0$ V), at various temperatures T. The data were collected between two contacts separated by a distance of about 2 μm. Near zero gate voltage, a strongly insulating state develops with a low-T resistance of about 120 MΩ. This huge resistance indicates successful elimination of edge state contributions[11,13]. By either warming the sample to near room temperature or applying a small gate voltage ($V_{tg} \approx 2.8$ V), a decrease of four orders of magnitude in R is observed, demonstrating the strongly insulating nature of the monolayer in the undoped regime. To characterize the insulator better, we performed four-probe resistance measurements (Fig. 1c). The resistance, R_{4p}, plotted on an Arrhenius scale at various values of V_{tg} can be treated as two regimes separated by a transition temperature near 100 K. By fitting the curve at $V_{tg} \approx -0.33$ V to the activation model, $R_{4p}(T) \propto \exp(\Delta/2k_BT)$, where k_B is the Boltzmann constant,

[1]Department of Physics, Princeton University, Princeton, NJ, USA. [2]Department of Electrical Engineering, Princeton University, Princeton, NJ, USA. [3]Department of Chemistry, Princeton University, Princeton, NJ, USA. [4]Research Center for Functional Materials, National Institute for Materials Science, Tsukuba, Japan. [5]International Center for Materials Nanoarchitectonics, National Institute for Materials Science, Tsukuba, Japan. [6]These authors contributed equally: Pengjie Wang, Guo Yu, Yanyu Jia. ✉e-mail: sanfengw@princeton.edu

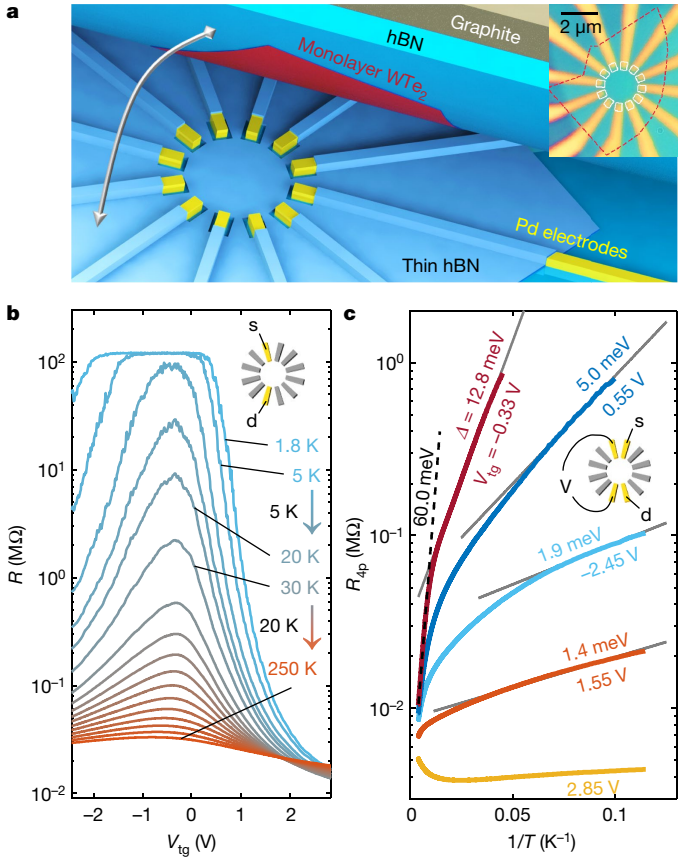

Fig. 1 | Device schematic and the insulating state of monolayer WTe_2. **a**, Cartoon illustration of the device design, where a thin hBN layer (blue) with selectively etched areas is used to avoid contact of the Pd electrodes (yellow) with the edges of the monolayer WTe_2. The stack of graphite (grey)/hBN (blue)/monolayer WTe_2 (red), shown in the cross-sectional view, is further stacked onto the bottom part with the electrodes, as indicated by the arrow. Inset, an image of device 1: the dashed red line highlights the monolayer edges and the white squares denote the contact regions. **b**, Gate-dependent two-probe resistance (R), taken from device 1, at various temperatures. V_{tg}, top-gate voltage. Inset, the measurement geometry (s, source; d, drain). **c**, Temperature dependence of the four-probe resistance (R_{4p}) at selected values of V_{tg}; inset, measurement geometry. Grey solid (black dashed) lines are the fits to the thermal activation model in the low (high) temperature regime. The extracted activation gaps (Δ) and V_{tg} are labelled next to the curves. Data taken from device 1.

we extract a gap $\Delta \approx 12.8$ meV in the low-T regime and $\Delta \approx 60.0$ meV in the high-T regime. The size of the gap is controlled by V_{tg} (Fig. 1c), as expected.

Quantum oscillations in the insulator

The magnetoresistance of this highly insulating phase exhibits strikingly large quantum oscillations (QOs). Figure 2a plots R as a function of magnetic field B applied perpendicular to the two-dimensional (2D) atomic plane, at $V_{tg} = -0.33$ V and $T = 1.8$ K. On top of the large background resistance, the oscillation starts to develop with an onset field, B_{onset}, as small as about 1.5 T. The oscillation component R_{osc} grows with increasing B, with an amplitude reaching approximately 60 MΩ near 8 T, about 2,300 times larger than the resistance quantum, h/e^2 (where h is the Planck constant, and e the electronic charge). Despite the material being such a strong insulator, the oscillation profile mimics Shubnikov–de Haas (SdH) oscillations in a good metal[20]. The QOs are robustly present in other devices (see Extended Data Fig. 2 for device 2 and Extended Data Figs. 3, 4 for device 3) and under different contact configurations (Extended Data Fig. 5), as well as in d.c. measurements (Extended Data Fig. 6). No QOs are observed under in-plane magnetic fields (Extended Data Fig. 7). Figure 2b plots the oscillations as a function of $1/B$, which shows a clear SdH-type periodicity. Applying a fast Fourier transform (FFT) to the curve yields a sharp peak α at an SdH frequency of approximately 48.6 T (Fig. 2c). If we adapt the standard analysis for SdH oscillations, this frequency indicates a quasiparticle density $n \approx 2.4 \times 10^{12}$ cm^{-2}, assuming a band with spin degeneracy. The oscillation profile, with many periods at a very small onset field, implies that the quasiparticles, which need to be fermions in order to give rise to the QOs, are highly mobile, with a mobility of the order of $1/B_{onset} \approx 6{,}000$ cm^2 V^{-1} s^{-1}.

To further characterize the QOs, we study their temperature dependence. Warming the device up to about 30 K washes out the oscillations (Fig. 2b) in device 1. In Fig. 2d we plot the normalized oscillation amplitude $\Delta R/R_0$ as a function of T, where R_0 is the zero-field resistance and ΔR is the peak-to-valley difference for a given oscillation period at selected B (Supplementary Information section S3). The curves deviate from the standard Lifshitz–Kosevich (LK) description[20] (dotted line) and display a saturation at low temperatures. The two-component LK formula, which describes contributions from two Fermi pockets, also fails to fit our data (dashed line). However, the data are well captured by a modified LK formula, $\Delta R/R_0 \propto \left[\frac{1}{\gamma(B)} + \frac{\sinh(\beta T m^*/B)}{e^{-D/B}\beta T m^*/B}\right]^{-1}$, where $\beta = 2\pi^2 k_B/(e\hbar)$ and $\hbar$ is the reduced Plank constant; m^* is the effective mass of the carriers; D describes the Dingle damping term and is related to the carrier mobility; and $\gamma(B)$ is a new term we introduce to describe the saturating behaviour at low T. Here we ascribe the fitting parameters to physical quantities according to the standard analysis of SdH oscillations in metals. The fits (solid lines in Fig. 2d; see also Supplementary Information section S3) yield $\gamma(B) \propto B^{\upsilon}$ with exponent $\upsilon \approx 3.0$, and a B-dependent effective mass m^* (see Fig. 2d inset). The corresponding cyclotron energy is estimated to be about 4.7 meV near the highest field in our measurements (9 T), where $m^* \approx 0.22 m_e$ (m_e is the free electron mass). At $B_{onset} \approx 1.5$ T, the cyclotron energy will be even smaller, and not comparable to the activation gap (Fig. 1c). The extracted quantum mobility μ is about 1,100 cm^2 V^{-1} s^{-1}, a high value as expected. The results indicate the possible existence of highly mobile fermions in the insulator. If these fermions were electrons or holes, a highly conductive sample would be expected, contradicting the observed strongly insulating behaviour.

This conflict can be reconciled if the fermions are assumed to be charge-neutral. Mobile neutral fermions can appear owing to electron fractionalization[1–3,21]. Indeed, the search for fractionalized Fermi surfaces occupied by neutral fermions has been a major experimental quest in strongly correlated quantum matter, such as quantum spin liquids[1,4,22,23]. Theoretically, despite being charge-neutral, these fermions (for example, spinons in spin liquids) may still couple to external magnetic fields through an internal gauge field and hence produce Landau quantization[4]. This concept has recently been extended to a different system, the mixed-valence insulators, in which a composite exciton Fermi liquid is proposed to exist[2,5]. QOs in resistivity are predicted to be observable on top of the activated charge transport[5], owing to the Ioffe–Larkin rule[24]. Interestingly, this theory indeed predicts the low-T saturation, which can be understood as a natural consequence of the unique B-dependent energy profile of neutral fermions[5].

Experimentally, evidence for QOs in insulators was reported only very recently in topological Kondo insulators under high magnetic fields[6,7] and InAs/GaSb quantum wells[25,26]. In contrast to our experiment, either no evidence for high mobility was extracted[6,7,25] or the sample remained conducting[26] (that is, resistance $\approx h/e^2$) in these previous experiments. Consequently, multiple theories based on charge carriers[27–34]—that is, involving Landau quantization of electronic bands outside the insulating gap—have been developed to capture the results of these experiments without invoking neutral fermions. Among them,

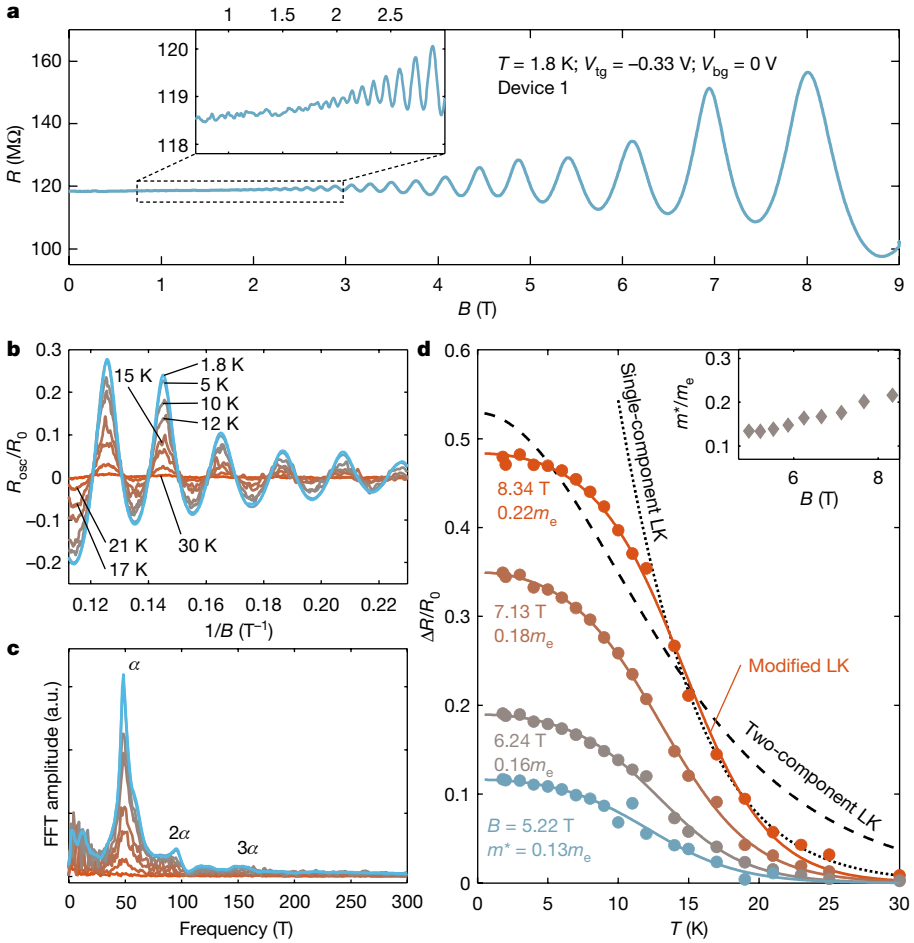

Fig. 2 | Quantum oscillations in the monolayer insulator. a, A typical low-temperature magnetoresistance curve taken in the insulating plateau of device 1. The magnetic field B is perpendicular to the 2D atomic plane; V_{bg}, bottom-gate voltage. Inset, zoomed-in view of the low-field data. **b**, Temperature dependence of the oscillating component R_{osc}, normalized by the zero-field resistance R_0, as a function of $1/B$. **c**, FFT of the same magnetoresistance data, showing a pronounced peak (labelled as α). Its second (2α) and third (3α) harmonics are also seen. **d**, Lifshitz–Kosevich (LK) fittings to the temperature-dependent oscillations at selected B. Inset, the extracted effective mass. See main text for an overview, and Supplementary Information section S3 for details of the fitting procedures.

several proposals predict QOs to appear in magnetization but not in charge transport[29–33], and hence they are not compatible with our observations. Thermal activation has been discussed as providing a channel for QOs to appear in resistivity[25,27,28,34]. However, we do not observe the proposed activated behaviour in our QOs and such activated charge carriers in insulators are not expected to exhibit high mobility. Thus, our results are inconsistent with existing scenarios based on charge carriers (see Methods for more discussions). More importantly, if the monolayer insulator indeed hosts highly mobile fermions, it may offer an unprecedented opportunity to examine the fully Landau quantized regime in an insulator, new territory that has been unexplored in all theories, including those involving neutral fermions.

The quantized regime

In Fig. 3, we summarize the key observations of another device (device 2), where we indeed observed a quantized regime. Figure 3a plots two-probe resistance R as a function of V_{bg}, taken at 2 K and at 500 mK. To provide better contact, V_{tg} is fixed at 2.5 V in this device. The highly insulating regime ($R > 1$ MΩ) is clearly developed when V_{bg} is less than −1.8 V. Compared to device 1, the measured resistance strongly fluctuates and has a lower value, indicating that additional residual charge carriers exist in this device, most probably owing to disorder and inhomogeneities. This is consistent with a large magnetoresistance seen at small fields (<1 T) in Fig. 3b (device 2) but absent in Fig. 2a (device 1), suggesting that these additional charge carriers in device 2 are rapidly localized. The sample also becomes as strongly insulating as device 1 when the field is applied. At 2 K, QOs appear at a similar B_{onset} (about 1.8 T; Fig. 3b), indicating a similar mobility to that of device 1. In Fig. 3b, c, the conductance G, defined as $1/R$, is plotted. Despite a lower oscillation frequency (about 23 T, Fig. 3b inset), the QOs here show results consistent with device 1, as summarized in Extended Data Figs. 2 and 8.

When device 2 is cooled down to 500 mK, B_{onset} shifts to an even smaller value, approximately 0.5 T (Fig. 3b inset), suggesting that the mobility is now much higher. Remarkably, at this temperature, the QOs develop into discrete peaks near 1.6 T, above which a quantized regime is fully developed (Fig. 3c). The data indicate that discrete Landau levels may be present inside the charge gap of the insulator. The low onset field of quantization and the evolving profile mimics the behaviour of high-mobility conventional 2D electron gases (2DEGs). The conductance peaks in the quantized regime are conventionally associated with individual Landau levels at the Fermi level. If the Landau level were occupied by charge carriers, for example, electrons or holes, the conductivity of the sample would be no different from other 2DEGs at this condition, that is, the sample would be highly conducting at the peaks. However, the monolayer remains a strong charge insulator at all fields and the measured peak resistances remain of the order of approximately 100 MΩ (Fig. 3c). Our experiments here clearly rule out existing QO theories based on charge carriers and favour the presence of neutral fermions in the insulator.

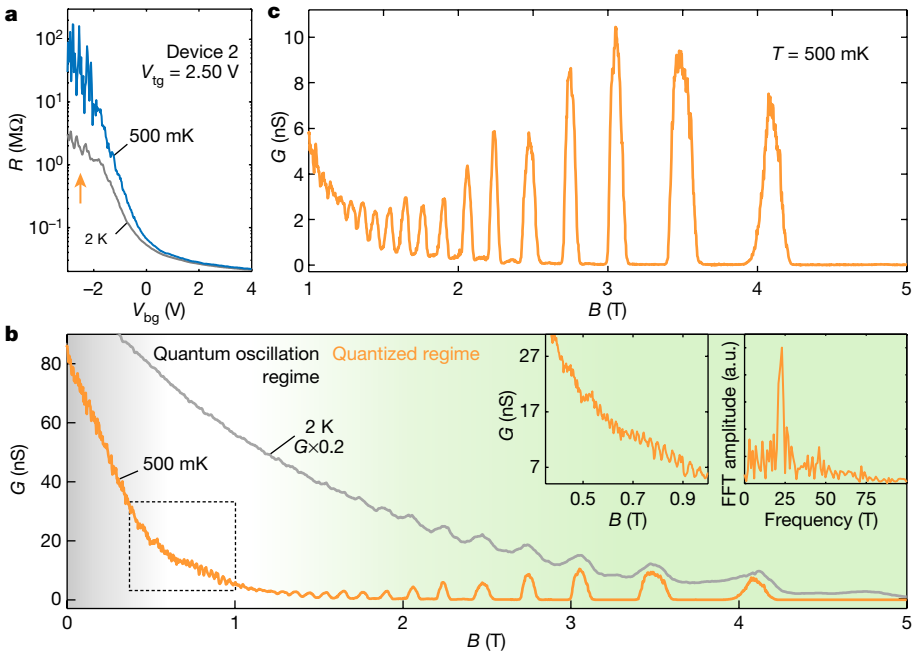

Fig. 3 | Quantized regime and discrete Landau levels in the monolayer insulator. a, Two-probe resistance R, taken from device 2, as a function of V_{bg} (V_{tg} = 2.5 V). **b**, Magnetic-field-dependent conductance G, defined as $1/R$, taken at a selected gate voltage (V_{bg} = −2.5 V, indicated by the arrow in **a**). Data taken at 500 mK (orange) clearly display the fully quantized regime (shaded with green), where discrete Landau levels are observed. Data at 2 K (grey curve) are shown as a reference. Left inset, zoomed-in view of the orange curve observed below 1 T, as indicated by the dashed box. Right inset, the FFT of the 500-mK data between 0.6 T and 1.5 T. **c**, Zoomed-in plot of the data above 1 T in **b**.

The effect of gate voltage

We next discuss gate-dependent studies, which provide additional insight into the observations. We note that the mobility of charge carriers in monolayer WTe_2 devices is typically low and, as a result, no QOs were observed in previous reports[11,13,18,19], even in the metallic regime. Indeed, Fig. 4a, b plots the magnetoresistance of devices 1 and 2, respectively, when the monolayer is electron-doped, and shows no QOs. Figure 4c presents a gate-tuned colour-map plot of R_{osc}/R_0 taken in device 1. Although strong oscillations appear in the insulating plateau, their amplitudes quickly diminish when the monolayer is doped with either holes or electrons. A careful examination (Extended Data Fig. 9) reveals hints of QOs towards the electron-doped regime but the QOs are very weak and only appear at the lowest measured temperature (1.8 K) in this device. In these devices with low charge mobilities, the QOs in the insulator are however very robust, as previously presented. To enhance the visibility of the metallic QOs, we have in device 3 optimized our fabrication procedure, including use of a flux-grown bulk WTe_2 crystal of exceptional quality. In this device, we achieved a substantial improvement in the mobility of charge carriers and hence can clearly resolve QOs, not only in the insulating regime but also in the metallic regime. We find very rich behaviours of multiple QO branches and clear correlations between the metallic and insulating branches. A systematic analysis of the observations in device 3 is presented in Methods and in Extended Data Figs. 3 and 4. Although a comprehensive understanding of these observations is currently lacking, in all devices we find that the mobility of gate-induced charge carriers is not related to the robustness of the QOs in the insulating regime.

The neutral fermion picture

Our experiments identify a variety of phenomena, in both the QO and fully quantized regimes, that point to the possible existence of highly mobile neutral fermions and neutral Fermi surfaces in the monolayer insulator. At this moment, the theory for such a neutral fermion picture in monolayer WTe_2 is yet to be developed. We mention two possible approaches. (1) Because the insulating state can be converted to a superconducting state with a low electron doping, proposals based on neutral Majorana fermions in failed superconductors[21,35] should be examined. (2) It is likely that a mechanism analogous to the formation of a composite exciton Fermi liquid[2,3,5] is applicable to monolayer WTe_2. In the second situation, electrons coexist with an equal number of holes, which, owing to correlations, split into charged bosonic holons and charge-neutral fermionic spinons (spin–charge separation). Coulomb attraction binds electrons and holons to form fermionic excitons, leaving behind a charge gap and mobile neutral fermions—that is, spinons and fermionic excitons[2]. We note that in semimetallic WTe_2 trilayers, QOs reveal that electrons and holes coexist at similar densities[15], and early calculations on the monolayer also predict the coexistence of electrons and holes[10]. In a separate paper[36], we present experimental evidence that supports the presence of an excitonic insulator phase in monolayer WTe_2, based on a systematic study combining transport and tunnelling measurements as well as theoretical modelling. We note that the reduced dimensionality and in-plane anisotropy, as well as the monolayer lattice being a distorted version of the dice lattice[37], could set the stage for strong correlations and the spin–charge separation.

Conclusion

The results presented here call for future investigations of the highly unusual insulating ground state of monolayer WTe_2 by both theory and experiment, and encourage the search for fractionalized, neutral Fermi surfaces inside this material's charge insulating gap. Further explorations in the quantized regime hold promise for advances in understanding the exact nature of the insulator. The connections between the possible fractionalized insulating phase and superconductivity, as well as non-trivial topology, deserve careful study, for which monolayer WTe_2 provides an excellent platform. We believe that the experimental search for quantum phases of neutral fermions, even beyond the Fermi surface state, will lead to a new chapter in quantum matter.

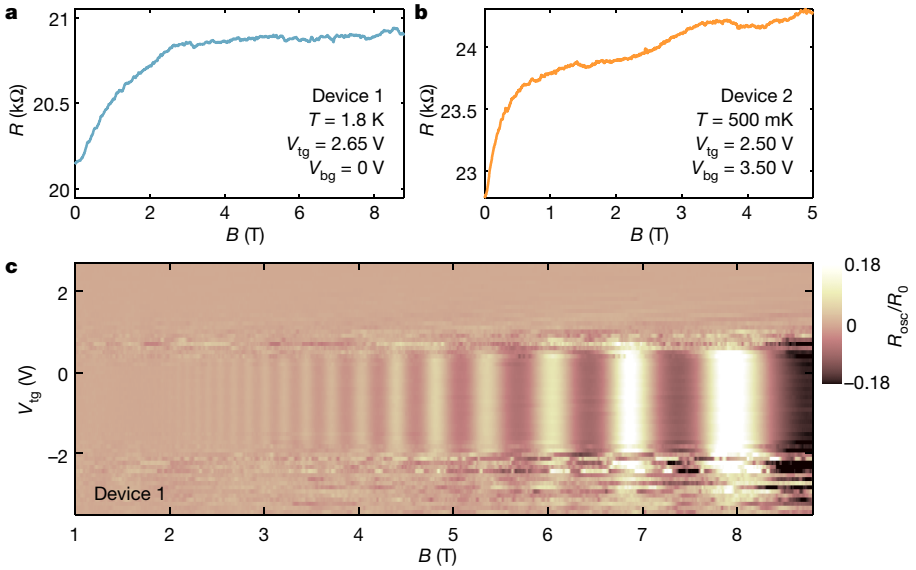

Fig. 4 | Gate dependence of the quantum oscillations. a, A typical magnetoresistance curve measured from device 1 when the monolayer is electron-doped by gating. **b**, A similar plot to **a**, but taken from device 2. The slight wiggles in the curves are probably due to disorder. Both show the absence of QOs. **c**, Colour map of the normalized oscillating component, R_{osc}/R_0, under varying B and V_{tg}, taken from device 1 at 1.8 K.

Online content

Any methods, additional references, Nature Research reporting summaries, source data, extended data, supplementary information, acknowledgements, peer review information; details of author contributions and competing interests; and statements of data and code availability are available at https://doi.org/10.1038/s41586-020-03084-9.

1. Zhou, Y., Kanoda, K. & Ng, T.-K. Quantum spin liquid states. *Rev. Mod. Phys.* **89**, 025003 (2017).
2. Chowdhury, D., Sodemann, I. & Senthil, T. Mixed-valence insulators with neutral Fermi surfaces. *Nat. Commun.* **9**, 1766 (2018).
3. Barkeshli, M., Nayak, C., Papić, Z., Young, A. & Zaletel, M. Topological exciton Fermi surfaces in two-component fractional quantized Hall insulators. *Phys. Rev. Lett.* **121**, 026603 (2018).
4. Motrunich, O. I. Orbital magnetic field effects in spin liquid with spinon Fermi sea: possible application to κ-$(ET)_2Cu_2(CN)_3$. *Phys. Rev. B* **73**, 155115 (2006).
5. Sodemann, I., Chowdhury, D. & Senthil, T. Quantum oscillations in insulators with neutral Fermi surfaces. *Phys. Rev. B* **97**, 045152 (2018).
6. Tan, B. S. et al. Unconventional Fermi surface in an insulating state. *Science* **349**, 287–290 (2015).
7. Xiang, Z. et al. Quantum oscillations of electrical resistivity in an insulator. *Science* **362**, 65–69 (2018).
8. Sato, Y. et al. Unconventional thermal metallic state of charge-neutral fermions in an insulator. *Nat. Phys.* **15**, 954–959 (2019).
9. Zibrov, A. A. et al. Tunable interacting composite fermion phases in a half-filled bilayer-graphene Landau level. *Nature* **549**, 360–364 (2017).
10. Qian, X., Liu, J., Fu, L. & Li, J. Quantum spin Hall effect in two-dimensional transition metal dichalcogenides. *Science* **346**, 1344–1347 (2014).
11. Fei, Z. et al. Edge conduction in monolayer WTe_2. *Nat. Phys.* **13**, 677–682 (2017).
12. Tang, S. et al. Quantum spin Hall state in monolayer 1T′-WTe_2. *Nat. Phys.* (2017).
13. Wu, S. et al. Observation of the quantum spin Hall effect up to 100 kelvin in a monolayer crystal. *Science* **359**, 76–79 (2018).
14. Ali, M. N. et al. Large, non-saturating magnetoresistance in WTe_2. *Nature* **514**, 205–208 (2014).
15. Fatemi, V. et al. Magnetoresistance and quantum oscillations of an electrostatically tuned semimetal-to-metal transition in ultrathin WTe_2. *Phys. Rev. B* **95**, 041410(R) (2017).
16. Zheng, F. et al. On the quantum spin Hall gap of monolayer 1T′-WTe_2. *Adv. Mater.* **28**, 4845–4851 (2016).
17. Song, Y.-H. et al. Observation of Coulomb gap in the quantum spin Hall candidate single-layer 1T′-WTe_2. *Nat. Commun.* **9**, 4071 (2018).
18. Fatemi, V. et al. Electrically tunable low-density superconductivity in a monolayer topological insulator. *Science* **362**, 926–929 (2018).
19. Sajadi, E. et al. Gate-induced superconductivity in a monolayer topological insulator. *Science* **362**, 922–925 (2018).
20. Shoenberg, D. *Magnetic Oscillations in Metals* (Cambridge Univ. Press, 2009).
21. Erten, O., Chang, P.-Y., Coleman, P. & Tsvelik, A. M. Skyrme insulators: insulators at the brink of superconductivity. *Phys. Rev. Lett.* **119**, 057603 (2017).
22. Motrunich, O. I. Variational study of triangular lattice spin-1/2 model with ring exchanges and spin liquid state in κ-$(ET)_2Cu_2(CN)_3$. *Phys. Rev. B* **72**, 045105 (2005).
23. Lee, S.-S. & Lee, P. A. U(1) gauge theory of the Hubbard model: spin liquid states and possible application to κ-$(BEDT\text{-}TTF)_2(Cu)_2(CN)_3$. *Phys. Rev. Lett.* **95**, 036403 (2005).
24. Ioffe, L. B. & Larkin, A. I. Gapless fermions and gauge fields in dielectrics. *Phys. Rev. B* **39**, 8988–8999 (1989).
25. Han, Z., Li, T., Zhang, L., Sullivan, G. & Du, R.-R. Anomalous conductance oscillations in the hybridization gap of InAs/GaSb quantum wells. *Phys. Rev. Lett.* **123**, 126803 (2019).
26. Xiao, D., Liu, C.-X., Samarth, N. & Hu, L.-H. Anomalous quantum oscillations of interacting electron-hole gases in inverted type-II InAs/GaSb quantum wells. *Phys. Rev. Lett.* **122**, 186802 (2019).
27. Shen, H. & Fu, L. Quantum oscillation from in-gap states and a non-Hermitian Landau level problem. *Phys. Rev. Lett.* **121**, 026403 (2018).
28. Zhang, L., Song, X.-Y. & Wang, F. Quantum oscillation in narrow-gap topological insulators. *Phys. Rev. Lett.* **116**, 046404 (2016).
29. Grubinskas, S. & Fritz, L. Modification of the Lifshitz-Kosevich formula for anomalous de Haas–van Alphen oscillations in inverted insulators. *Phys. Rev. B* **97**, 115202 (2018).
30. Ram, P. & Kumar, B. Theory of quantum oscillations of magnetization in Kondo insulators. *Phys. Rev. B* **96**, 075115 (2017).
31. Knolle, J. & Cooper, N. R. Quantum oscillations without a Fermi surface and the anomalous de Haas–van Alphen effect. *Phys. Rev. Lett.* **115**, 146401 (2015).
32. Knolle, J. & Cooper, N. R. Excitons in topological Kondo insulators: theory of thermodynamic and transport anomalies in SmB_6. *Phys. Rev. Lett.* **118**, 096604 (2017).
33. Knolle, J. & Cooper, N. R. Anomalous de Haas–van Alphen effect in InAs/GaSb quantum wells. *Phys. Rev. Lett.* **118**, 176801 (2017).
34. Pal, H. K., Piéchon, F., Fuchs, J.-N., Goerbig, M. & Montambaux, G. Chemical potential asymmetry and quantum oscillations in insulators. *Phys. Rev. B* **94**, 125140 (2016).
35. Baskaran, G. Majorana Fermi sea in insulating SmB_6: a proposal and a theory of quantum oscillations in Kondo insulators. Preprint at http://arXiv.org/abs/1507.03477v1 (2015).
36. Jia, Y. et al. Evidence for a monolayer excitonic insulator. Preprint at http://arXiv.org/abs/2010.05390 (2020).
37. Sutherland, B. Localization of electronic wave functions due to local topology. *Phys. Rev. B* **34**, 5208–5211 (1986).

Methods

Sample fabrication

The WTe_2 bulk crystals were grown using methods similar to those described in previous work[14,38]. The exfoliation and search for hBN and graphite flakes were performed under ambient conditions. The sample contacts were patterned by electron beam lithography, followed by a cold develop, reactive ion etching, and metal deposition (3 nm Ti/17 nm Pd). The holes in the thin hBN for contacts were patterned by electron beam lithography and etched by reactive ion etching. The exfoliation, search and transfer of monolayer WTe_2 flakes were performed in a glovebox equipped with a dry transfer setup. Step-by-step sample fabrication procedures are illustrated in Extended Data Fig. 1 and Supplementary Information section S1.

Transport measurement

The electrical measurements of our devices were performed either in a cryostat (Quantum Design Dynacool) equipped with a superconducting magnet or in a dilution refrigerator (Bluefors LD250) equipped with a superconducting magnet. Standard lock-in measurements were taken with a low-frequency (<7 Hz) a.c. excitation (<5 mV). A current preamplifier (DL Instrument 1211) was used to improve signals.

Contact resistance

Our key resistance data were taken in two-probe measurements, which involve contact resistance. We note that the presence of contact resistance does not alter our conclusions because contact resistance is not expected to give rise to QOs. A large contact resistance can only lower the visibility of the QOs (that is, R_{osc}/R). Hence the fact that pronounced QOs are seen implies that the contact resistance is small compared to the sample resistance. The contact resistance may introduce a small correction to the LK fittings (Fig. 2d, Extended Data Fig. 8 and Supplementary Fig. 1), but the only impact would be a slight change of the extracted parameters (for example, the effective mass), which are not essential to our conclusions. One advantage of our device geometry is that the top gate can be used to improve the contact properties if the pristine version is not good enough.

Excluding trivial explanations

Here we add further discussion on excluding trivial scenarios involving unexpected contamination from any metallic regimes that may be present in the devices. The metallic components in our devices include edge states of the monolayer, graphite gates, metal electrodes and possible metallic islands in the monolayer due to impurities, bubbles and so on. We first note that our device is designed to avoid edge contributions: this is the key to observing the QOs (absent in previous devices involving edges). In addition, there is no known mechanism for 1D helical edge modes to give rise to QOs with periodicity in $1/B$. Next, we present systematic investigations of alternative explanations based on graphite. (1) Our graphite gates are well separated from the WTe_2 channel by the hBN dielectric. Within our applied gate range, no measurable leak current is presented (that is, the resistance between graphite and WTe_2 is above our measurement limit, >100 GΩ). However, the measured channel resistance in the QO regime is about 100 MΩ, suggesting that the current flow is restricted to the monolayer. The strict d.c. measurements, which show consistent QOs (Extended Data Fig. 6), indicate that the QO signal is unrelated to any unexpected capacitive coupling to the graphite. (2) The graphite is also not expected to develop QOs that are qualitatively similar to the ones observed in our devices, which are dominated by a single frequency (see a recent study[39], which shows that QOs developed in a thin graphite film, even if fully encapsulated by hBN on both top and bottom sides, are highly irregular below 10 T). Also, in our case, the thin graphite gates are not fully encapsulated and the graphite DOS are not expected to be fully gapped[39] in magnetic fields. (3) We have fabricated and measured three devices without using graphite gates (Extended Data Fig. 10). Although the quality of these devices is substantially lower than that of the graphite-gated devices, hints of magnetoresistance oscillation with $1/B$ periodicity were seen in the insulating regime in the sub-kelvin regime. (4) Owing to the capacitance effect between the two gates (especially when the monolayer WTe_2 is an insulator), a changing gate voltage (either the top or bottom gate) will inevitably tune the carrier density of both top and bottom graphite. Hence the unchanged frequency of the QO branches observed in devices 1 and 3 is inconsistent with assigning the QOs to the graphite layer. (5) Graphite gates have been widely used for 2D devices (for example, graphene or transition metal dichalcogenides) whose transport measurements do not show graphite QOs. Especially in the metallic regime of device 3 (with doping well above the metal–insulator transition, MIT), the situation in our devices is directly comparable to that of graphene devices. (6) The gate-tuned QOs observed in device 3 exhibit very rich behaviours, including the appearance of multiple branches, the rich dependence on the displacement field, the clear correlations between metallic and insulating branches, and an intermediate regime where QOs are absent (see next section). All these behaviours are unlikely to be attributable to a graphite artefact. Thus, we conclude that the observed QOs are due to the unusual intrinsic properties of the monolayer WTe_2.

In general, for any metallic channels to be responsible for the QOs, they cannot be in parallel with the monolayer insulator, since this would short the insulator and contradict the huge measured resistance. They cannot be in series with the monolayer insulator either, as the amplitude of SdH oscillations in metals is only expected to be of the order of h/e^2, which contradicts the large QO amplitude observed in our devices (for example, R_{osc} reaches about 60 MΩ in Fig. 2). QOs from a metallic regime in series are expected to be invisible on top of the huge background resistance. Moreover, in the quantized regime of device 2 (Fig. 3c), the zero conductance between peaks corresponds to a resistance reaching about 100 GΩ, implying that the contributions from any metallic regime have been completely suppressed. Our data cannot be explained by the presence of any metallic component listed above.

More analysis of device 3

In the main text, we have presented gate-dependent studies of the QO signals observed in device 1, where we have observed a dominant mode with a frequency at about 48.6 T and a slow modulation at approximately 13.2 T in the insulating state. A very weak branch appears towards electron doping only at the lowest measured temperature (1.8 K). The weakness (device 1) or absence (device 2) of QOs in the metallic regime indicates that the mobilities of charged carriers are low. In device 3 (see device image in Extended Data Fig. 3a), we have substantially improved the mobilities of charge carriers, by using an optimized fabrication method that minimizes disorder and a much-improved flux-grown WTe_2 bulk crystal (with an exceptional residual resistivity ratio of ~2,500). This improvement allows us to clearly resolve QOs not only in the insulator regime but also in the metallic regime.

We first compare device qualities in Extended Data Fig. 3b, by showing the resistance of devices 1–3 as a function of the gate-induced carrier density $n_g \equiv \varepsilon_r\varepsilon_0[(V_{tg}/d_{tg}) + (V_{bg}/d_{bg})]/e$, where e is the elementary charge, ε_r is the relative dielectric constant of hBN, ε_0 is the vacuum permittivity and d_{tg} (d_{bg}) is the thickness of the hBN layer associated with the top (bottom) gate. The data were taken at 70 K. One immediately sees that the resistance peak of device 3 is about an order of magnitude narrower than those of the other two, indicating substantially reduced disorder of charge carriers. The offset of the peak maximum (that is, the charge neutrality point, CNP) from zero n_g is another impurity indicator, as it reveals the unintentional doping during the fabrication process. This offset is also much reduced in device 3, again demonstrating its excellent quality. In Extended Data Fig. 3c, we show the temperature-dependent R_{4p}, revealing an MIT that occurs at $n_g \approx 2.4 \times 10^{12}$ cm^{-2}. In a separate manuscript[36], we present systematic studies of the transport properties of this device, including the dual-gated resistance map and Hall

response in a relatively high-temperature regime. The results there support the insulating state of monolayer WTe_2 as an excitonic insulator and rule out alternative explanations such as a band insulator or a localized insulator[36]. Here we focus on the QOs, which appear at low temperatures.

Extended Data Fig. 3e and f illustrates the QO frequency map under varying n_g at a selected displacement field D ($D \equiv [(V_{bg}/d_{bg}) - (V_{tg}/d_{tg})]\varepsilon_r/2$). The corresponding traces of the scanning n_g are illustrated in Extended Data Fig. 3d. The FFT amplitude is normalized to its individual maximum in each magnetoresistance curve at a given n_g to enhance the visibility of QOs at all gates. The data were taken at 7 K to minimize the bad contact regime. The QO map with $D \approx 0.15$ V nm^{-1} (a value we believe is needed to cancel the residual displacement field in the devices, that is, corresponding to zero net D; see more discussions in ref. [36]) clearly reveals an electron-like (e-like) branch in the electron-doped metallic regime and a hole-like (h-like) branch in the hole-doped regime (Extended Data Fig. 3e). Interestingly, near the CNP, an additional branch, labelled α_1, develops at a frequency of ~17 T. The appearance of this α_1 peak is consistent with the observation in device 1 (Extended Data Fig. 9). We note that while the flake quality is substantially improved here, the contact properties in the insulating regime are however worse than in device 1. Device 1 so far exhibits the best contact properties among all fabricated devices, which allows us to observe QOs without applying a top-gate voltage (that is, at CNP near $D = 0$, Extended Data Fig. 9). With $D = 0.59$ V nm^{-1}, more features develop as shown in Extended Data Fig. 3f. In the electron-doped regime, one additional h-like branch appears accompanied by an increased frequency of the e-like branch. In the insulating state near CNP, we now see two branches (α_2 and β). One branch, labelled α_2, appears at a frequency very close to that of α_1. The β branch appears at a location that is strongly correlated with the e- and h-like branches in the doped regime. We find that the β branch consistently shows up at the intersection of the e- and h-like traces if one extends them into the insulating regime; that is, the three branches (e, h and β) form a tilted "Y" shape (Extended Data Fig. 3g). The effect of the displacement field will be further discussed below. The observation suggests that the insulating β branch shares the same origin as the e- and h-like branches.

While the frequency of the β peak is gate-tunable, we next carefully examine the insulating α_2 branch and show that its frequency is gate-independent. A careful examination of the h-like branch shown in Extended Data Fig. 3f reveals an interesting wiggling behaviour near the frequency of α_2. This is due to the presence of an additional branch (α_3) in the metallic regime. To confirm its existence, we plot the QO frequency map under varying displacement field D at a fixed $n_g = 2 \times 10^{12}$ cm^{-2}. We observe that the frequencies of the e- and h-like branches increase with increasing D. This displacement field effect is consistent with the expectation that the application of D to the WTe_2 monolayer enlarges the Fermi surface of both electrons and holes without altering the total charge density (see more experimental and theoretical discussions in ref. [36]). Clearly, in addition to the e- and h-like branches, branches located near the α_2 frequency develop in the map (Extended Data Fig. 4a). We have identified these α branches by labelling them as α_3–α_6. Their emergence appears to be correlated with the e- or h-like branches. For instance, it looks like the α_3 and α_6 branches may arise due to a splitting associated with the h-like branch as one increases D. Interestingly, once the α branches develop, the gate voltages have only a very weak or no impact on their frequency. To further reveal the gate dependence of the α_3 branch, we plot its behaviour when varying the voltage of a single gate (V_{tg} or V_{bg}) while fixing the other (Extended Data Fig. 4b and c). It is clear that neither gate is able to tune the frequency of the α_3 branch. This α_3 branch is in fact the one that produces the wiggling behaviour in the h-like branch in Extended Data Fig. 3g. Also, this α_3 branch is correlated to the insulating α_2 branch. To examine the gate voltage dependence of the α_2 branch, in Extended Data Fig. 4f, we fix the charge density at the CNP and vary the displacement field D (that is, the two gate voltages are varied in opposite directions). The map clearly reveals a gate-tunable β branch and a gate-independent α_2 branch. In Extended Data Fig. 4g, we summarize the appearance of the α branches in the measured maps.

Although a comprehensive understanding of the existence and gate-voltage dependence of these QO branches is currently lacking, we make several comments on the observations. (1) The observation of the gate-voltage-independent α branch in device 3 is consistent with device 1 (Extended Data Fig. 9), where the observed insulating branches (despite the presence of two frequencies) show no dependence on the applied top-gate voltage. (2) One important difference between the two devices is the measurement regime in the parameter space spanned by n_g and D. Device 1 exhibited the best contact properties among all our fabricated devices and it is so far the only device that allows us to perform measurements in the insulating regime without applying a top-gate voltage (for example, $V_{tg} = 0$ V, or near $D = 0$ at the CNP, Fig. 4c). In all other devices including device 3 shown here, we have to apply a finite V_{tg} in order to achieve good contacts. In particular, we do not have QO information around the CNP near $D = 0$ for device 3. The contact issue needs to be considered when comparing different devices. (3) The appearance of both e- and h-like branches is remarkably consistent with the excitonic insulator picture for the insulating state[36]. (4) We note that there is also an intermediate regime below the MIT where all QOs are absent (Extended Data Fig. 3g). This could indicate a non-trivial interacting effect of the correlated electron–hole system near the transition. (5) In Extended Data Fig. 4b and c, the e- and h-branches appear to be individually controlled by the top and bottom gates in the doped regime. This is consistent with the expectation that both the capacitance effect and the displacement field effect come into play when one tunes a single gate voltage. For example, increasing V_{tg} will lead to an increasing magnitude of D as well as an increasing n_g. If D enlarges both e- and h- pockets (see discussions in ref. [36]) while n_g enlarges the e-pocket yet reduces the h-pocket, then a net result can be that only the e-pocket size is enlarged. The effect can also be understood in real space, as shown in Extended Data Fig. 4e. With the applied gate voltages, the presence of a finite D will polarize the electron and hole distributions in the out-of-plane direction (note that the WTe_2 monolayer is made of three atomic layers). In this case, the top gate couples to the electron layer while the bottom gate couples to the hole layer, naturally producing the gate dependence seen in Extended Data Fig. 4b and c. (6) We further emphasize that the gate response of an excitonic insulator is a rather complicated process, which is distinct from that of a simple system like graphene. For instance, in a correlated electron–hole system, the system can adjust either the hole or the electron concentration in response to the same change of the total charge density. As shown in ref. [40], even in a simplified model of an artificial electron–hole bilayer system, the gate response is highly non-trivial. The exact response of an excitonic insulator further depends on microscopic details including correlations and disorders. In our case, the electrons and holes are much more confined in a single WTe_2 layer, where strong electron–hole correlations are expected. The highly unusual ground state of monolayer WTe_2 (probably the excitonic insulating ground state) is the key to understanding the various observations presented here.

Data availability

The data that support the findings of this study are available at Harvard Dataverse (https://doi.org/10.7910/DVN/KQNDDQ) or from the corresponding author upon reasonable request.

38. Ali, M. N. et al. Correlation of crystal quality and extreme magnetoresistance of WTe_2. *Europhys. Lett.* **110**, 67002 (2015).
39. Yin, J. et al. Dimensional reduction, quantum Hall effect and layer parity in graphite films. *Nat. Phys.* **15**, 437–442 (2019).
40. Zeng, Y. & MacDonald, A. H. Electrically controlled two-dimensional electron-hole fluids. *Phys. Rev. B* **102**, 085154 (2020).

Acknowledgements S.W. is indebted to N. P. Ong and A. Yazdani for their support for his new laboratory and their encouragement and discussions regarding this work. We acknowledge discussions with B. A. Bernevig, D. Cobden, F. D. M. Haldane, P. Jarillo-Herrero, P. A. Lee, T. Senthil, I. Sodemann, S. Sondhi and X. Xu. This research was supported primarily by NSF through the Princeton University Materials Research Science and Engineering Center (DMR-1420541) and a CAREER award to S.W. (DMR-1942942). Early measurements were performed at the National High Magnetic Field Laboratory, which is supported by NSF Cooperative Agreement no. DMR-1644779 and the State of Florida. K.W. and T.T. acknowledge support from the Elemental Strategy Initiative conducted by the MEXT, Japan, grant no. JPMXP0112101001, JSPS KAKENHI grant no. JP20H00354 and the CREST (JPMJCR15F3), JST. F.A.C. and R.J.C. acknowledge support from the ARO MURI on Topological Insulators (grant W911NF1210461). S.L, S.K. and L.M.S. acknowledge support from the Arnold and Mabel Beckman Foundation through a Beckman Young Investigator grant awarded to L.M.S and the Gordon and Betty Moore Foundation through grant GBMF9064 to L.M.S.

Author contributions P.W., G.Y., Y.J. and M.O. fabricated devices and built measurement systems. P.W., G.Y., Y.J. and S.W. performed measurements and analysed data. S.W. designed and supervised the project. F.A.C., R.J.C., S.L., S.K. and L.M.S. grew and characterized bulk WTe_2 crystals. K.W. and T.T. provided hBN crystals. S.W. and P.W. wrote the paper with input from all authors.

Competing interests The authors declare no competing interests.

Additional information

Supplementary information is available for this paper at https://doi.org/10.1038/s41586-020-03084-9.

Correspondence and requests for materials should be addressed to S.W.

Peer review information *Nature* thanks Johannes Knolle, Feng Miao and the other, anonymous, reviewer(s) for their contribution to the peer review of this work.

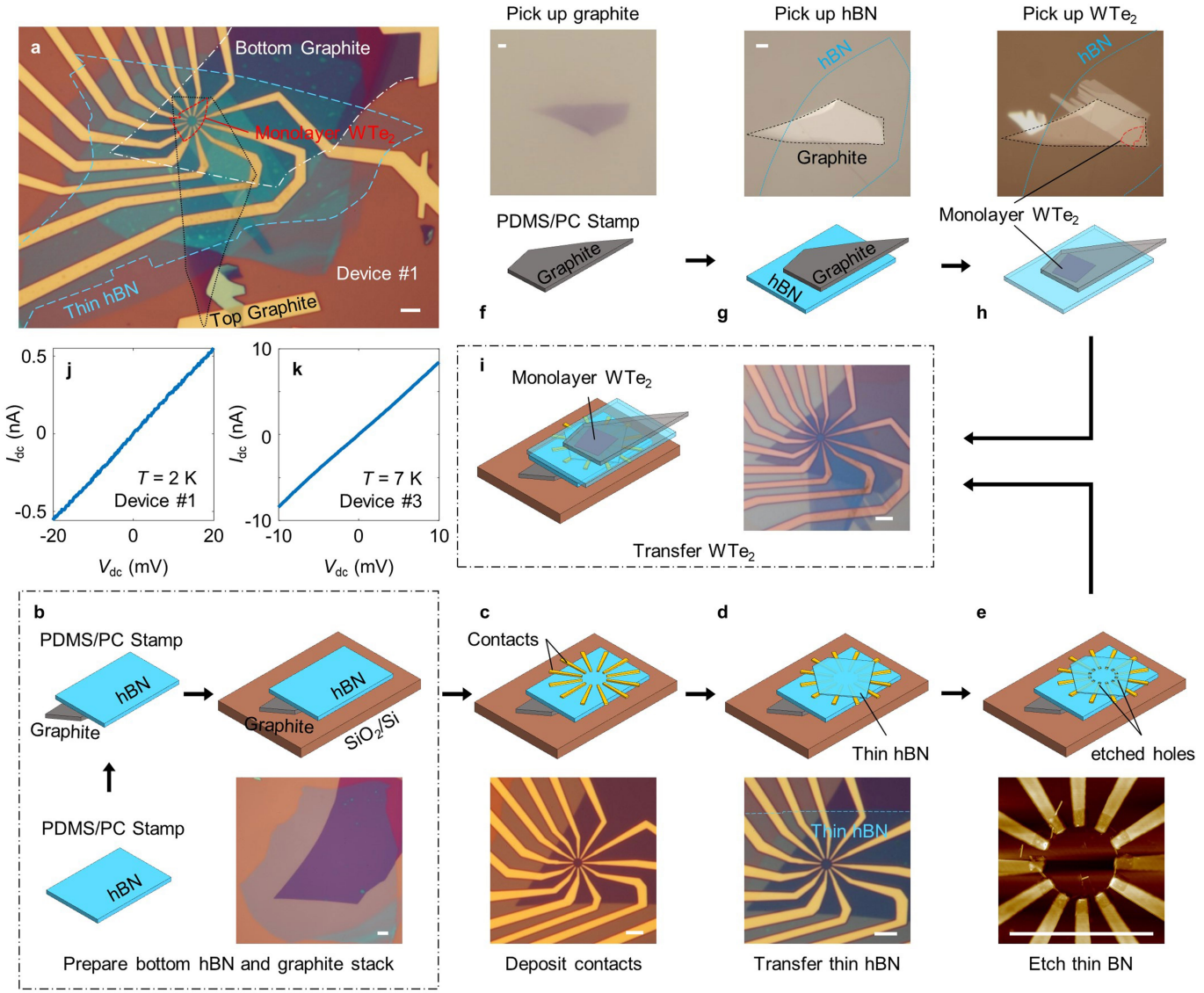

Extended Data Fig. 1 | Sample fabrication process. a, An optical image of device 1. The monolayer WTe_2 is highlighted by the red dashed line. **b**, Bottom hBN and graphite preparation. **c**, Deposition of metal contacts (3 nm Ti and 17 nm Pd). **d**, Transfer of thin hBN in a dry transfer system under ambient conditions. **e**, Etching thin hBN at the tips of the electrodes. **f**, Picking up the top graphite. **g**, Picking up the top hBN. **h**, Picking up monolayer WTe_2. Images in **g** and **h** are taken by flipping over the stamp after picking up the flakes. No visible bubbles are observed. **i**, Transfer of monolayer WTe_2 to the prefabricated bottom part of the sample prepared in **b**–**e**. **j**, **k**, Typical *I*–*V* curves (d.c. measurement) of device 1 (**j**) and device 3 (**k**) between two contacts at 1.8 K and 7 K respectively, showing ohmic behaviour. All scale bars, 4 μm. Detailed information about the sample fabrication is presented in Supplementary Information section S1.

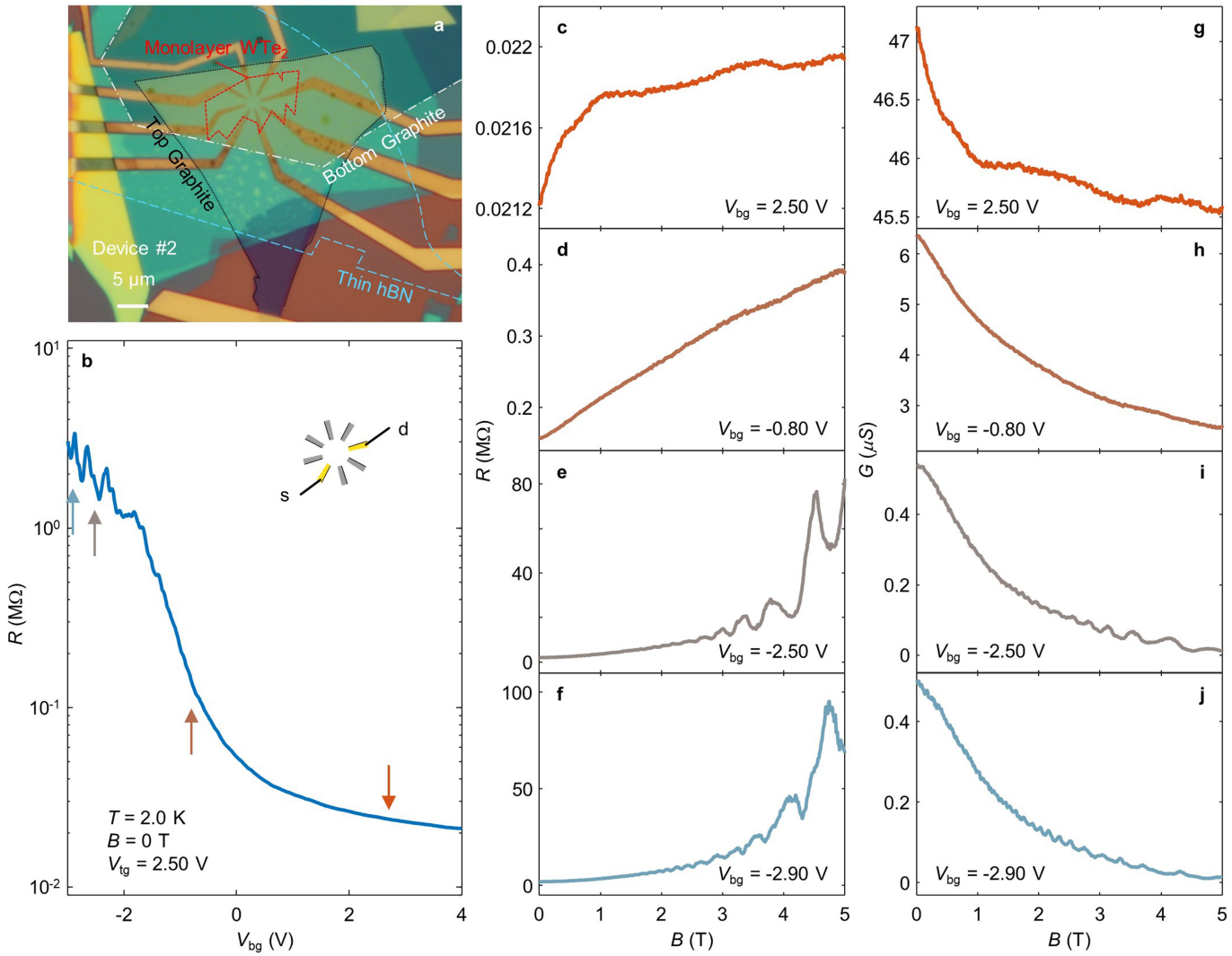

Extended Data Fig. 2 | Summarized data from device 2. a, An optical image of device 2. The red dashed line highlights monolayer WTe_2. **b**, Gate-dependent two-probe resistance *R*. The inset shows the measurement geometry. The coloured arrows indicate the gate voltages used in **c**–**f**. **c**–**f**, Raw data of the magnetoresistance curves taken at selected V_{bg}: **c**, 2.50 V; **d**, −0.80 V; **e**, −2.50 V; **f**, −2.90 V. Strong QOs are observed in the insulating regime but disappear when the monolayer is doped. **g**–**j**, The same data as in **c**–**f**, but plotted in *G*.

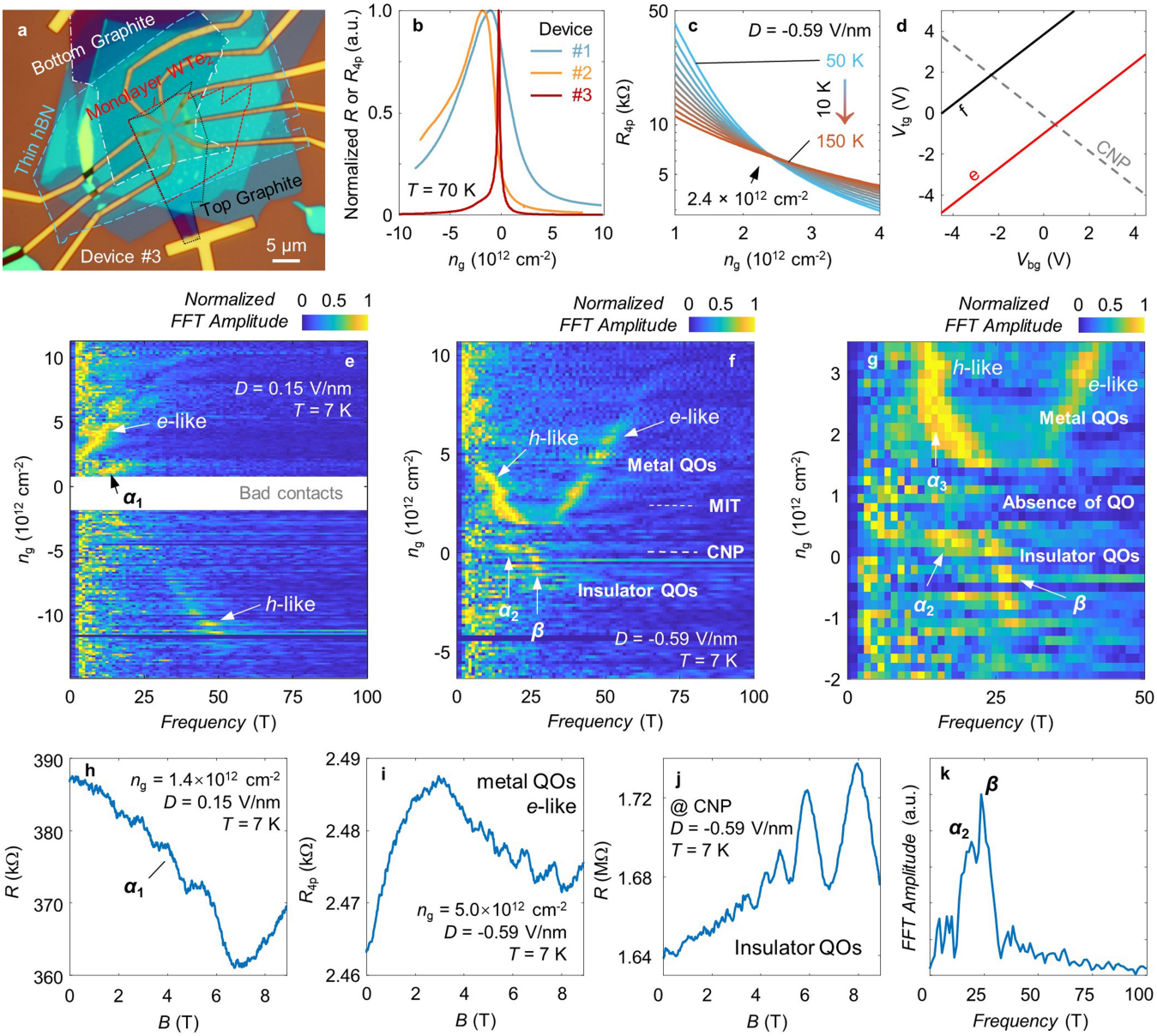

Extended Data Fig. 3 | Quantum oscillations observed in device 3 with high charge-carrier mobility. a, An optical image of device 3. The red dashed line highlights monolayer WTe_2. **b**, Comparison of the gate-tuned resistance of the three devices at 70 K (normalized R_{4p} for devices 2 and 3, and normalized R for device 1). See Methods for definition of n_g. **c**, Gate-tuned R_{4p} of device 3 with a fixed $D = -0.59\ \mathrm{V\,nm^{-1}}$ ($D \equiv (V_{bg}/d_{bg} - V_{tg}/d_{tg})\varepsilon_r/2$)), showing the metal–insulator transition (MIT) at $n_g \approx 2.4 \times 10^{12}\ \mathrm{cm^{-2}}$, indicated by the arrow. **d**, Schematic diagram of gate-tuning traces used in **e** (red) and **f** (black), along which lines D is fixed while n_g is varied. The dashed line indicates the CNP. **e**, Normalized FFT amplitude of the QOs under varying n_g at $D = 0.15\ \mathrm{V\,nm^{-1}}$ (see Methods for discussion of D and of the normalization of FFT amplitude). In addition to the e-like and h-like QO branches, an additional branch α_1 appears near CNP. **f**, n_g-tuned FFT amplitude (normalized) of the QOs at $D = -0.59\ \mathrm{V\,nm^{-1}}$. QOs in both the metallic (e-like and h-like branches) and the insulating regime (α_2 and β branches) are clearly observed. **g**, Zoomed-in plot of the FFT features near the CNP in **f**, highlighting the correlations between the insulating and metallic branches. **h**, The magnetoresistance trace corresponding to the α_1 branch in **e** ($n_g = 1.4 \times 10^{12}\ \mathrm{cm^{-2}}$ and $D = 0.15\ \mathrm{V\,nm^{-1}}$). **i**, The magnetoresistance trace (R_{4p}) of the metallic QO branch in **f** ($n_g = 5.0 \times 10^{12}\ \mathrm{cm^{-2}}$ and $D = -0.59\ \mathrm{V\,nm^{-1}}$). **j**, Magnetoresistance (R) trace taken at CNP with $D = -0.59\ \mathrm{V\,nm^{-1}}$, showing QOs in the insulating phase. **k**, FFT of the oscillation component in **j**. Discussions of these observations are presented in Methods.

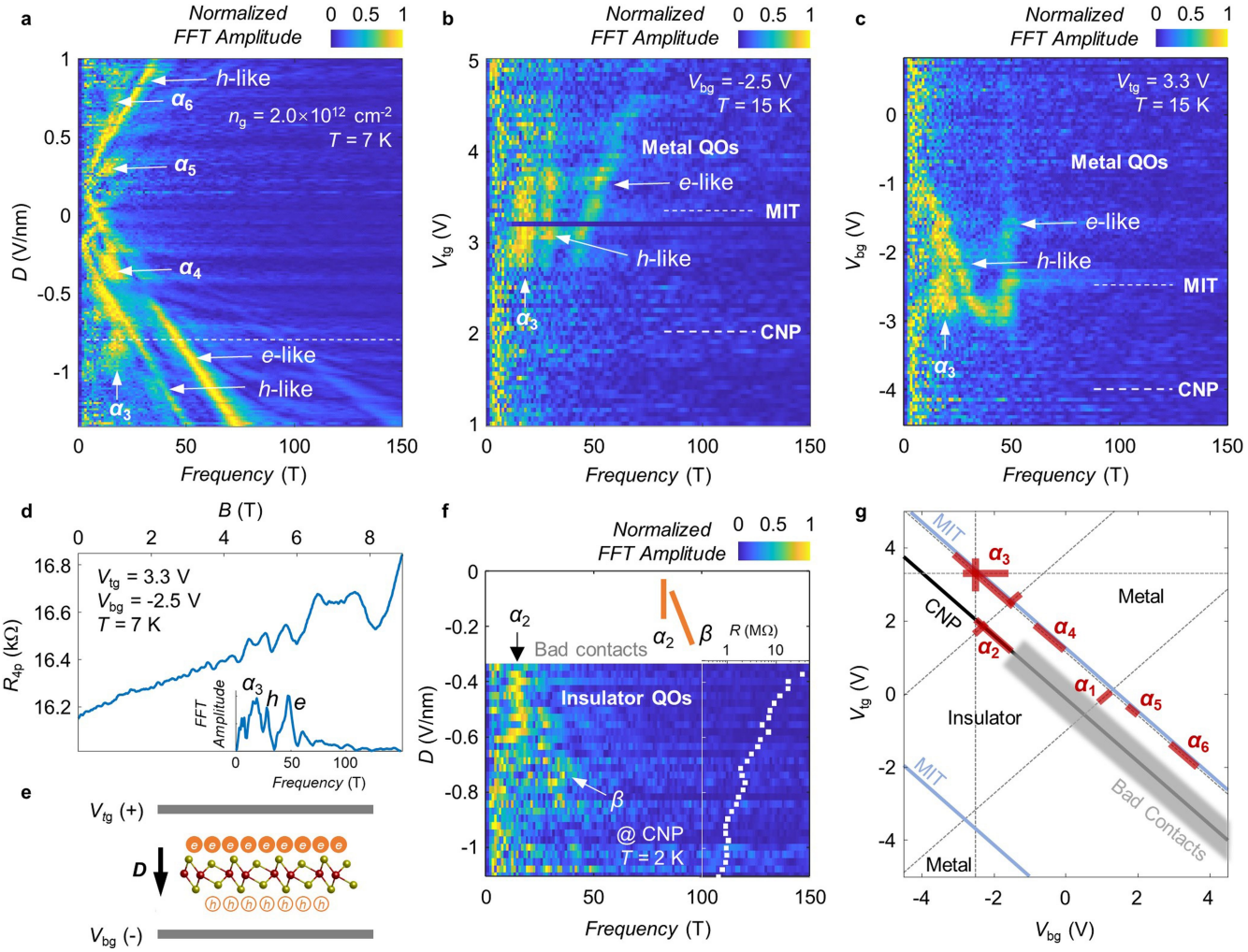

Extended Data Fig. 4 | Further investigation of the quantum oscillations reported in Extended Data Fig. 3. a, *D*-tuned QO frequency map (normalized) at $n_g = 2.0 \times 10^{12}$ cm^{-2} and $T = 7$ K. Visible branches (α_3–α_6, e-like and h-like) are noted. **b**, V_{tg}-tuned QO frequency map at $V_{bg} = -2.5$ V and $T = 15$ K. **c**, V_{bg}-tuned QO frequency map at $V_{tg} = 3.3$ V and $T = 15$ K. Three visible branches of QOs in **b** and **c** are labelled as α_3, h-like and e-like. At $T = 15$ K, no QOs are observed in the insulator regime. **d**, Raw data of the QOs at $V_{tg} = 3.3$ V and $V_{bg} = -2.5$ V, corresponding to the dashed line in **a**. Inset, the FFT of the oscillating amplitude, showing three peaks as labelled. **e**, Illustration of monolayer WTe_2, showing the geometry of top and bottom gates. The presence of the displacement field polarizes the electron distribution. This results in the separation of electrons and holes, which can then couple to the top and bottom gates, respectively. **f**, *D*-dependence of the insulator QOs (α_2 and β branches) at the CNP ($T = 2$ K). Inset, the corresponding resistance at zero *B* (the resistance increases further with *B*), confirming the insulating nature. The behaviours of the α_2 and β branches are also sketched (solid orange lines). **g**, A sketch summarizing the appearance of the gate-independent α branches (α_1–α_6) on the maps that we have presented. Grey dashed lines, traces that were examined. Blue solid lines, MIT. Black solid line, CNP. Grey area, bad contact region (where information about QOs is inaccessible in our measurement). Discussions of these observations are presented in Methods.

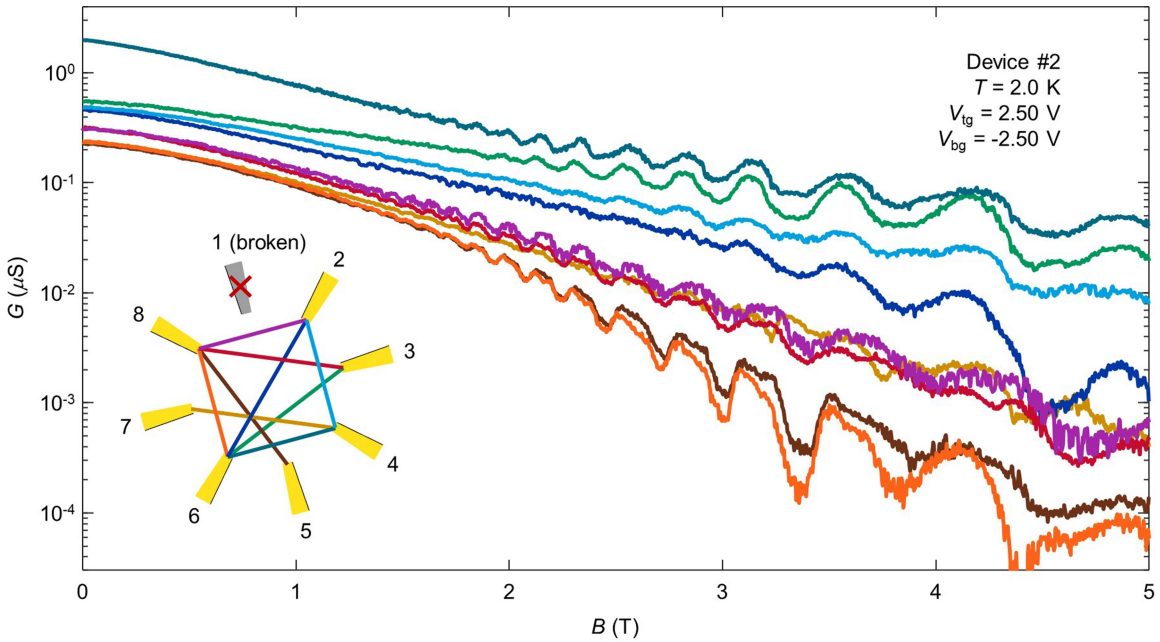

Extended Data Fig. 5 | Quantum oscillations observed when using different contact configurations in device 2. The QOs are robustly observed between various contact pairs connected to the monolayer WTe_2 flake. In this device, 7 out of 8 contacts are working (contact 1 was broken during fabrication). Inset, the contact pairs for each data curve. For each coloured data curve, the source and drain contacts are indicated by connecting them with a solid line of the same colour. The data curves were taken individually, that is, all other contacts were disconnected when one pair of contacts was chosen to be measured. Data were recorded at 2 K.

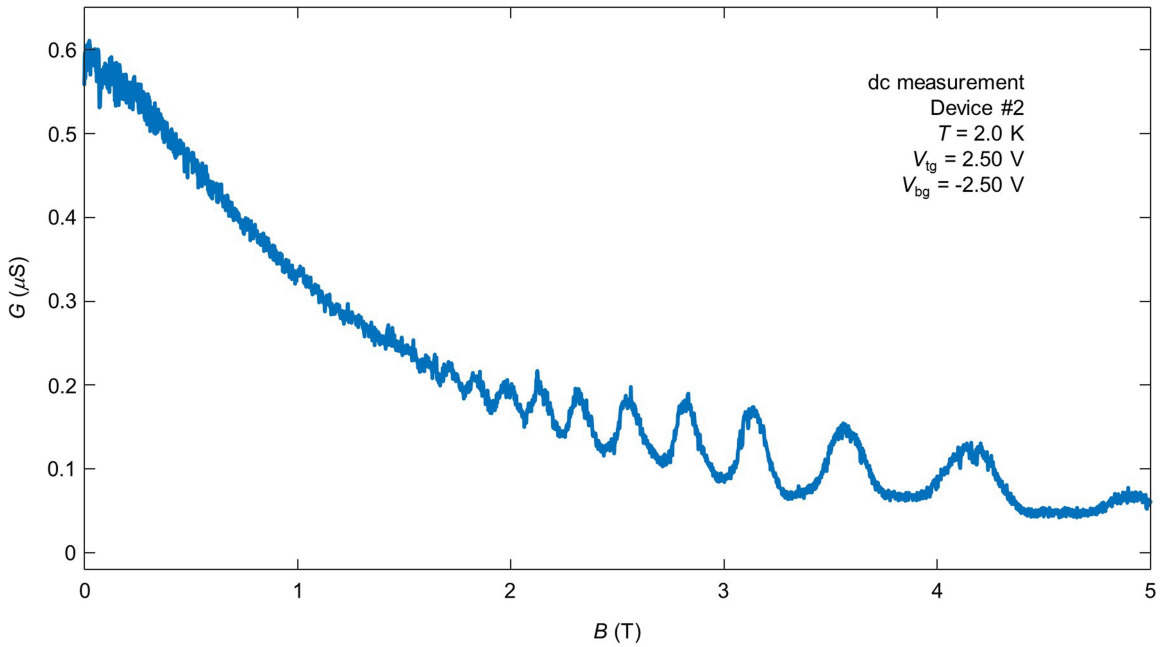

Extended Data Fig. 6 | Quantum oscillations observed in d.c. measurements. The two-probe d.c. conductance (G) as a function of the magnetic field B was measured by applying a small d.c. excitation with an amplitude of 1.5 mV via a Keithley 2400 while monitoring the d.c. current. This strict d.c. measurement yields results consistent with the low-frequency a.c. measurement reported in the main text. Data were taken at 2 K from a pair of contacts in device 2.

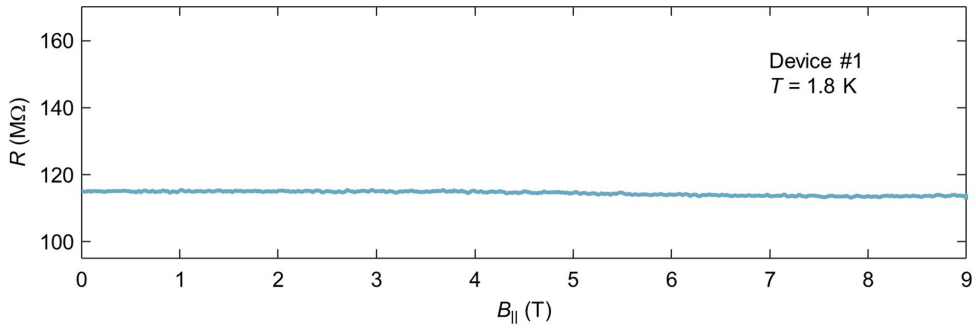

Extended Data Fig. 7 | The effect of an in-plane magnetic field on the resistance. The two-probe resistance (R) as a function of the magnetic field $B_{||}$ applied in the atomic plane of the monolayer WTe_2. Data were taken in device 1 using the same two contacts used in Fig. 2, in the insulating plateau at T = 1.8 K.

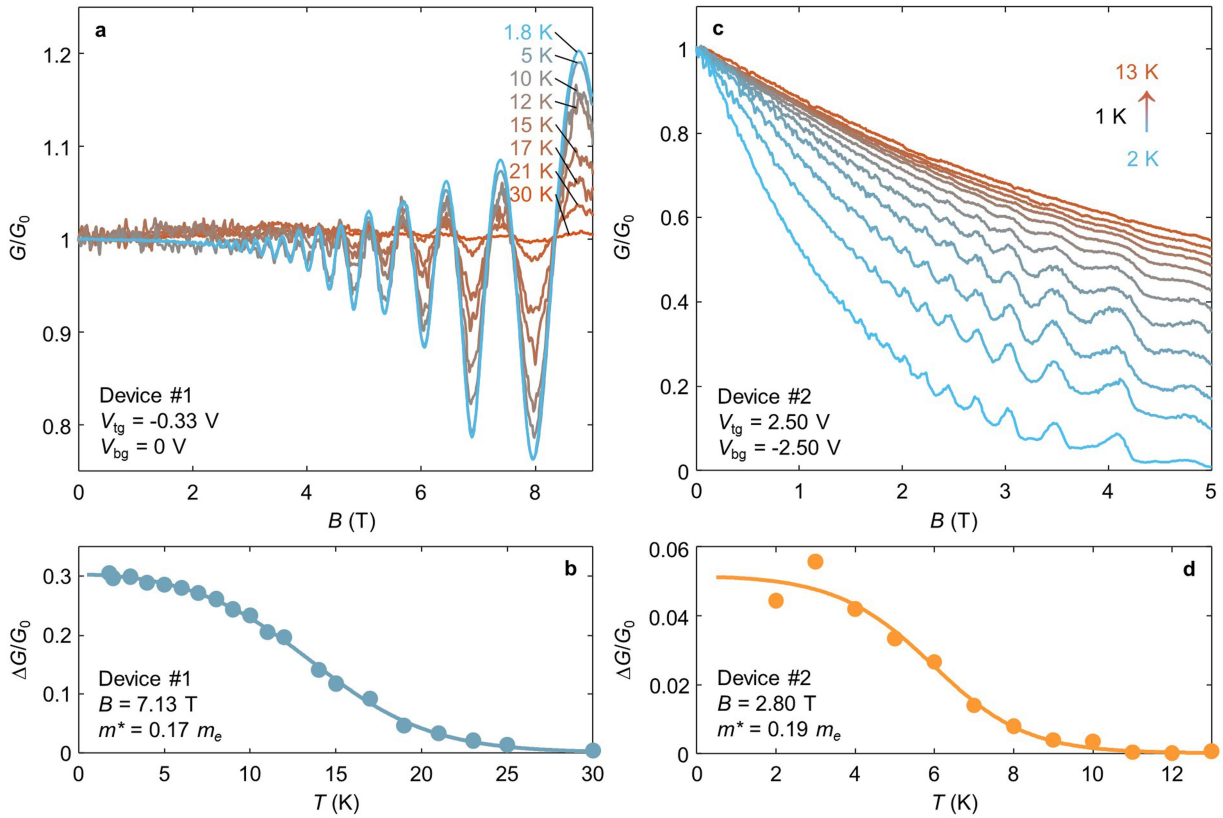

Extended Data Fig. 8 | Additional analysis of the quantum oscillations in devices 1 and 2. a, Temperature dependence of conductance $G \equiv 1/R$ for device 1, normalized by its zero-field conductance. The same data set was used in Fig. 2, in which R is plotted instead of G. **b**, Temperature-dependent oscillating amplitude at a selected field (7.13 T) for device 1. The solid line is the fit based on the modified LK formula described in the main text. Values of the fitting parameters extracted here are similar to those from the analysis in Fig. 2. **c**, **d**, Conductance data and LK fitting for device 2.

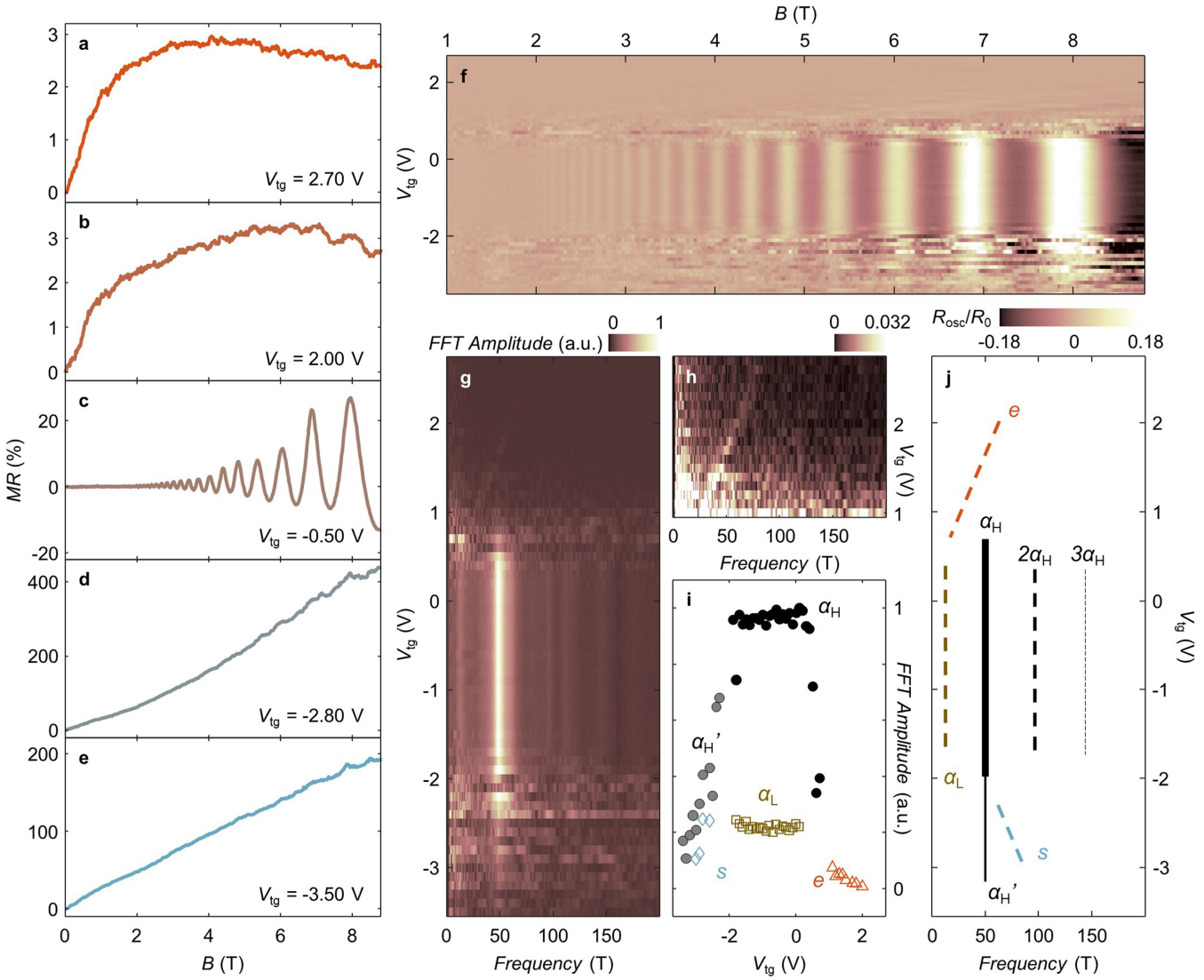

Extended Data Fig. 9 | The effect of gating on the quantum oscillations in device 1. a–**e**, Magnetoresistance (MR ≡ $(R(B) - R_0)/R_0$) curves taken at selected V_{tg} (V_{bg} = 0 V). **f**, Colour map of the normalized oscillating component, R_{osc}/R_0, under varying B and V_{tg}. **g**, FFT map of the same data. **h**, A zoomed-in plot of the FFT map at $V_{tg} > 1$ V, highlighting the weak peak that features a gate-tunable frequency. **i**, Gate-dependent FFT amplitudes of all visible peaks. **j**, A sketch summarizing the observed peaks. The solid black line (α_H peak, corresponding to the α peak mentioned in the main text) is the most pronounced peak and the focus of our discussion. Dashed coloured lines are weak features, whose amplitudes are shown in **i**. In the insulating regime, a lower-frequency peak (α_L) emerges together with the α_H peak. Towards the hole side, the α_H peak splits into two peaks (α_H' and s). Towards the electron side, a new peak (e) emerges from almost zero frequency with an amplitude that decreases monotonically. Coincident with the emergence of the e peak, the amplitudes of the α_H and α_L peaks drop abruptly. Careful studies of these weak modes under higher magnetic fields and lower temperatures may provide further information to help the understanding of this system. Data were recorded from a pair of contacts in device 1, at 1.8 K.

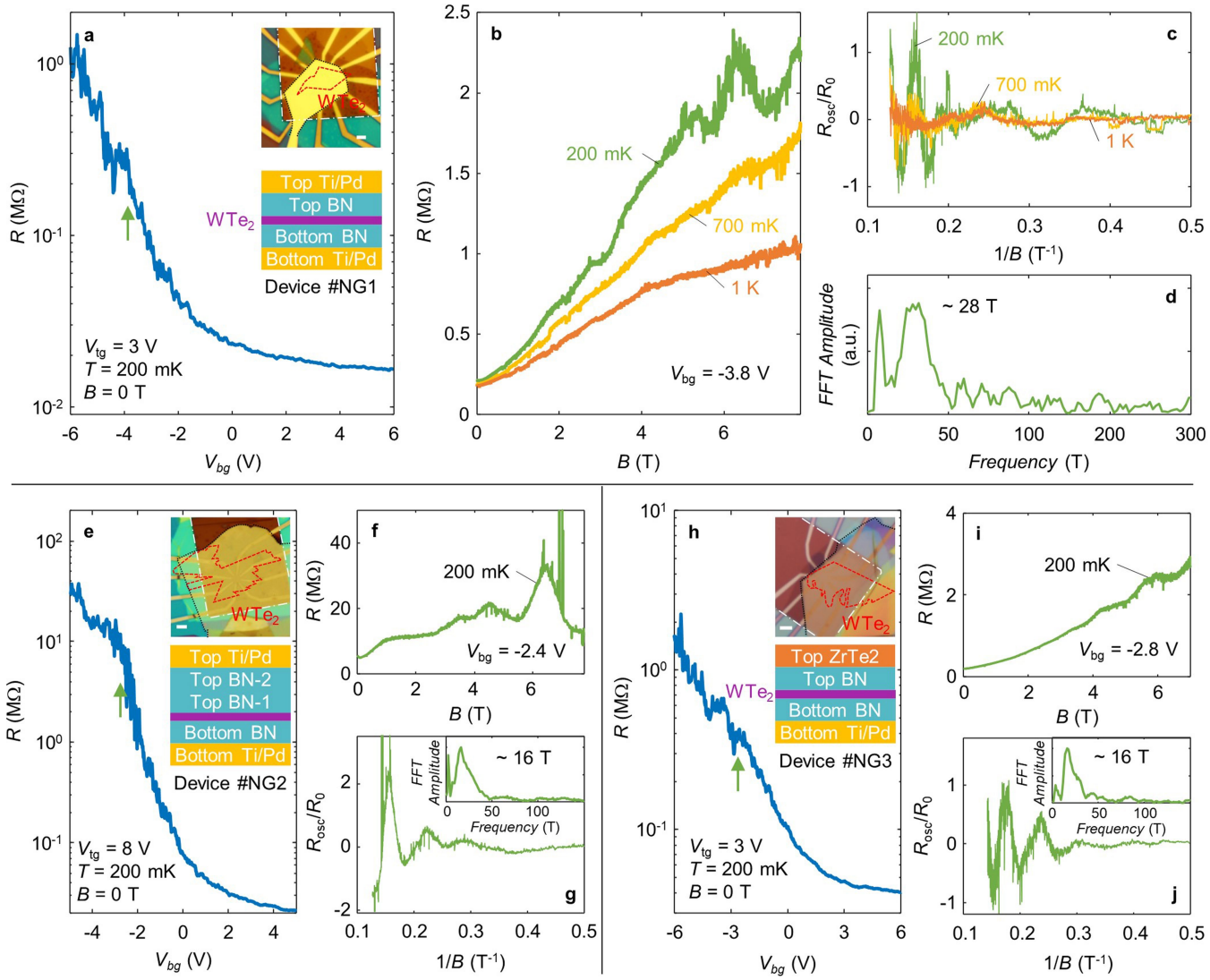

Extended Data Fig. 10 | Magnetoresistance oscillations in non-graphite-gated devices. a, Two-probe resistance (R) measured for device NG1 as a function of the bottom-gate voltage (V_{bg}) at a fixed top-gate voltage (V_{tg}). Inset, the device image and layer schematic. **b**, The magnetoresistance at a fixed V_{bg}, corresponding to a location indicated by the green arrow in **a**. The oscillations are visible at 200 mK but disappear at higher temperatures. **c**, The normalized oscillating component of the magnetoresistance (R_{osc}/R_0) shown in **b** after background extraction. **d**, FFT of the 200 mK curve in **c**. **e**, Gate-dependent R and device information for another non-graphite-gated device, NG2. Inset, the device image and layer schematic. **f**, A magnetoresistance trace observed in the insulating regime (location indicated by the green curve in **e**). **g**, Its oscillation component together with the FFT (inset). **h**–**j**, The same summary as **e**–**g** but for device NG3. The top gate is replaced by a thin $ZrTe_2$ flake, which is air-sensitive and its degradation could introduce inhomogeneities to the WTe_2 channel. We note that in all three devices, the observed sample resistances are lower than our typical graphite devices. Higher top-gate voltages are also needed for the metal top-gated devices in order to perform measurements in the insulating regime (that is, we expect substantial contact resistance in the measured curves). Magnetoresistance oscillations only develop in the sub-kelvin regime, indicating that freezing out the excess charge carrier is perhaps important to their appearance. All scale bars in the device images are 3 μm.